Volume 27
Number 41
7 November 2025
Pages 6689–6838

CrystEngComm

rsc.li/crystengcomm

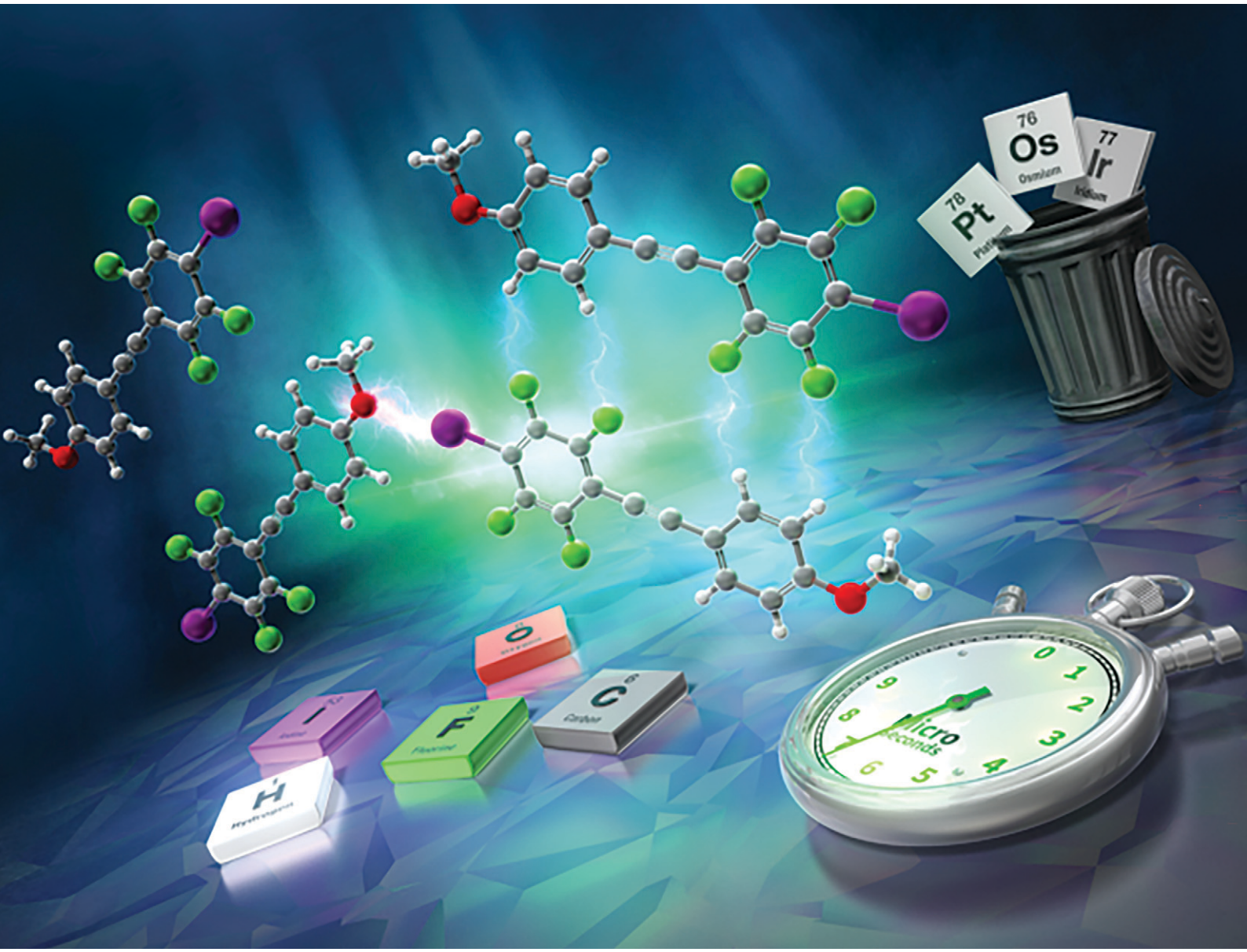

ISSN 1466-8033

ROYAL SOCIETY OF CHEMISTRY

PAPER

Masato Morita, Shigeyuki Yamada *et al.*
Interplay of C–H···F and halogen bonding interactions for tunable room-temperature phosphorescence in iododiphenylacetylene systems

CrystEngComm

ROYAL SOCIETY OF CHEMISTRY

PAPER

View Article Online
View Journal | View Issue

Cite this: *CrystEngComm*, 2025, **27**, 6735

Interplay of C–H···F and halogen bonding interactions for tunable room-temperature phosphorescence in iododiphenylacetylene systems†

Masato Morita, *[a] Motohiro Yasui, [b] Tsutomu Konno [b] and Shigeyuki Yamada *[b]

Received 10th July 2025,
Accepted 16th September 2025

DOI: 10.1039/d5ce00690b

rsc.li/crystengcomm

Efficient room-temperature phosphorescence (RTP) often depends on specific intermolecular interactions, such as C–H···F and halogen bonding interactions; however, their role in fluorinated diphenylacetylene derivatives remains unclear. In this study, we systematically synthesized a series of iododiphenylacetylene derivatives containing fluorine or methoxy substituents to elucidate the relationships between intermolecular interactions, molecular packing, and RTP properties. Single-crystal X-ray diffraction and cyclic voltammetry were employed to investigate their packing structures and estimate the electronic properties, respectively, and their photophysical properties were examined. Both C–H···F and halogen bonding interactions contributed to enhancing RTP; however, C–H···F interaction induced by fluorine atoms played a more significant role in increasing the phosphorescence intensity and efficiency. Moreover, the combination of both intermolecular interactions resulted in a synergistic improvement in RTP properties. These findings provide valuable guidelines for designing and developing efficient diphenylacetylene-based RTP materials.

Introduction

Organic light-emitting materials are commonly applied in various devices, including organic light-emitting diodes (OLEDs),[1–3] organic field-effect transistors,[4–8] organic lasers,[9–11] and sensing devices.[12,13] Among them, phosphorescent materials that utilize triplet excitons offer a higher theoretical efficiency in OLEDs than in their fluorescent counterparts.[14] However, triplet excitons are easily deactivated at room temperature, inhibiting efficient phosphorescence. To overcome this challenge, precious metals, such as Ir and Pt, can be incorporated into the structure of luminophores to promote intersystem crossing *via* the heavy-atom effect.[15,16] Although this approach has successfully enabled room-temperature phosphorescence (RTP), growing interest in sustainability and cost reduction has prompted the development of metal-free phosphorescent systems, particularly using organic RTP materials.[17,18] Tang *et al.* reported the phenomenon of aggregation-induced emission, subsequently resulting in the concept of crystallization-induced phosphorescence (CIP).[19–21] They revealed that molecular motion can be suppressed in the crystalline state by leveraging various intermolecular interactions, such as C–H···F interaction, halogen bonding, and CH/π interactions. Thus, their study provided valuable design guidelines for the development of efficient RTP molecules.

In addition to CIP, co-crystallization using organic materials has emerged as a promising strategy for achieving efficient RTP.[22] For example, Agostino *et al.* reported that co-crystals formed between diphenylacetylene (**DPA**) and diiodotetrafluorobenzene (in 1 : 1 or 1 : 2 molar ratios) *via* C–I···π interactions exhibited efficient RTP. In particular, the 1 : 2 co-crystals completely suppressed fluorescence, resulting in enhanced RTP.[23] Additionally, **DPA** exhibits ultralong phosphorescence when its two aromatic rings adopt a highly twisted conformation.[24,25] These promising phosphorescent properties of **DPA** inspired us to further explore **DPA**-based RTP materials.

We previously reported that a fluorinated **DPA** derivative, compound **1**, exhibited efficient RTP in crystalline states (Scheme 1a).[26] Because compound **1** comprises iodine and methoxy groups at both longitudinal ends, the efficient RTP was attributed to a combination of intermolecular interactions, such as C–H···F interaction and halogen bonding, and the heavy-atom effect of the iodine atom. The valuable role of the heavy-atom effect of iodine is well

[a] *Graduate School of Science and Engineering, Ibaraki University, 4-12-1 Nakanarusawa, Hitachi, Ibaraki 316-8511, Japan*
[b] *Faculty of Molecular Chemistry and Engineering, Kyoto Institute of Technology, Matsugasaki, Sakyo-ku, Kyoto 606-8585, Japan. E-mail: syamada@kit.ac.jp*

† Dedicated to Professor Resnati, celebrating a career in fluorine and noncovalent chemistry on the occasion of his 70th birthday.

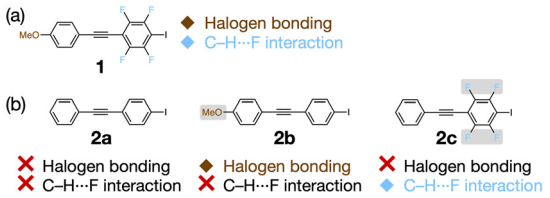

Scheme 1 (a) **DPA**-based RTP molecule previously reported by our group. (b) Target molecules used in this study.

established; however, the relative contributions of C–H···F and halogen bonding interactions to the RTP properties of compound **1** remain unclear, rendering clarification of this issue essential to rationally design efficient **DPA**-based RTP materials.

In this study, we synthesized a series of iododiphenylacetylene derivatives, **2a–c**, and evaluated their crystal structures and photophysical properties to elucidate the relationships between intermolecular interactions, molecular packing, and RTP properties (Scheme 1b). The target compounds were as follows: **2a**, with only an iodine atom (to isolate the heavy-atom effect);[27] **2b**, with both an iodine atom and methoxy group (to enable halogen bonding);[28] and **2c**, with iodine and fluorine substituents on the same aromatic ring (to enable C–H···F interaction *via* fluorine).[29,30] Detailed analyses using single-crystal X-ray diffraction (SCXRD) and the photophysical properties of **2a–c** revealed that C–H···F interactions *via* fluorine atoms play a more significant role in enhancing RTP than halogen bonding or the heavy-atom effect alone. Furthermore, the combined presence of C–H···F and halogen bonding interactions improved the RTP properties of the **DPA** derivatives. These findings provide valuable insight into the molecular design of **DPA**-based RTP materials.

Experimental

Materials and methods

The ^{1}H-NMR (400 MHz) and ^{13}C-NMR (100 MHz) spectra were obtained using a Bruker AVANCE III 400 NMR spectrometer in a chloroform-*d* ($CDCl_3$) solution. The chemical shifts were reported in parts per million (ppm) using residual protons in the NMR solvent. The ^{19}F-NMR (376 MHz) spectra were obtained using a Bruker AVANCE III 400 NMR spectrometer in a $CDCl_3$ solution with $CFCl_3$ (δ_F = 0 ppm) as the internal standard. All chemicals, including the solvents, were of reagent grade and purified as typical prior to use. Column chromatography was conducted on silica gel (Fujifilm Wako Pure Chemical Corporation, Wakogel® 60 N, 38–100 μm), and thin-layer chromatography (TLC) was performed on silica gel TLC plates (Merck, Silica gel 60F_{254}).

Crystal growth

The single crystals of **2a–c** were obtained *via* recrystallisation from a mixed solvent (dichloromethane/methanol = 1 : 1). Approximately 100 mg of **2a–c** was dissolved in 5 mL of the mixed solvent and was slowly evaporated over five days in a loosely capped screw vial.

Single-crystal X-ray diffraction

SCXRD was performed using a Rigaku XtaLAB AFC11 diffractometer. The reflection data were integrated, scaled, and averaged using the Rigaku CrysAlisPro program (ver. 1.171.39.43a). Empirical absorption corrections were performed using the SCALE 3 ABSPACK scaling algorithm (CrysAlisPro). The structures were identified using a direct method (SHELXT-2018/2)[31] and refined using the full-matrix least-squares method (SHELXL-2018/3)[32] visualized using Olex2.[33]

Cyclic voltammetry

Cyclic voltammetry (CV) measurements were performed using an ECstat-101 potentiostat (EC Frontier, Kyoto, Japan) with glassy carbon, Pt, and Ag/AgCl as the working, counter, and reference electrodes, respectively. Ferrocene (Fc)/ferrocenium (Fc^+) was used as an external reference, while tetrabutylammonium hexafluorophosphate (Bu_4NPF_6) was used as the supporting electrolyte (0.1 mol L^{-1}). All measurements were performed following argon bubbling for 30 min in a 1 × 10^{-3} mol L^{-1} acetonitrile solution at a scan rate of 50 mV s^{-1}. The highest occupied molecular orbital (HOMO) and lowest unoccupied molecular orbital (LUMO) energy levels were estimated from the onset potentials of the oxidation (E_{Ox}) and reduction (E_{Red}) waves (*versus* Fc/Fc^+) using the following equations: $E_{HOMO} = -4.80 - E_{Ox}$, $E_{LUMO} = -4.80 - E_{Red}$, and $\Delta E = E_{LUMO} - E_{HOMO}$.

Photophysical properties

UV-vis absorption spectra were recorded using a JASCO V-530 absorption spectrometer, and the photoluminescence (PL) spectra of the solutions and crystals were recorded using a JASCO FP-6600 fluorescence spectrometer. The absolute quantum yields of the solutions and crystals were measured using a Hamamatsu Photonics Quantaurus-QY system (C11347-01). The PL lifetime was measured using a Hamamatsu Photonics Quantaurus-Tau lifetime spectrometer (C11367-34).

Results and discussion

Single-crystal X-ray diffraction

The packing structures of compounds **2a–c** were confirmed using SCXRD. As shown in Fig. 1a, compound **2a** crystallized in the monoclinic *P*2 space group, with eight molecules per unit cell. Although compound **2a** is an achiral molecule, it crystallized in the chiral space group *P*2. Such spontaneous resolution can occur when directional intermolecular interactions, such as C–H···F interaction, guide the molecules into a chiral packing arrangement.[34] In particular, the **DPA** cores adopted a zig-zag herringbone-type arrangement. This packing is supported by multiple short contacts between the C–H bonds of one molecule and the aromatic ring of an adjacent molecule with C–H···Cg

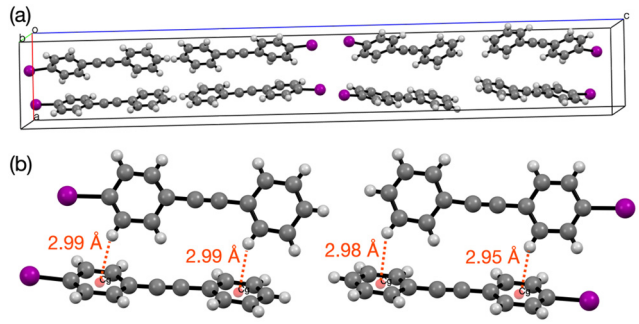

Fig. 1 Crystal structure of **2a**: (a) unit cell and (b) molecular packing involving C–H···Cg short contacts.

distances of 2.95–2.99 Å (Fig. 1b, Cg = centroid of the aromatic ring). No significant π–π stacking interactions were observed.

Compound **2b** crystallized in an orthorhombic $Pca2_1$ space group, with four molecules per unit cell (Fig. 2a). Similar to that for **2a**, **2b** exhibited a herringbone-type packing structure. This arrangement is supported by a C–H/π interaction, characterized by an H···Cg distance of 2.83 Å and a C–H···Cg angle of 136.4° (Fig. 2b). In addition, halogen bonding connects adjacent molecules *via* a C–I···O contact of 3.23 Å. The geometry of this bond, with a C–I···O angle of 172.7° and I···O–C angle of 128.2°, confirmed a directional σ-hole interaction. The overall molecular conformation of **2b** is highly similar to that of **2a**.

The crystal structure of compound **2c** has already been reported (CCDC 245724), which was determined at 100 K.[30] To enable a systematic and direct comparison of the molecular packing and intermolecular interactions at room temperature, we re-determined the crystal structure of compound **2c** at 298 K. As a result, compound **2c** was found to belong to the monoclinic $P2_1/n$ space group, with four molecules in a unit cell (Fig. 3a). Unlike that for non-fluorinated **2a** and **2b**, the packing of **2c** is dominated by π-stacking interaction and C–H···F

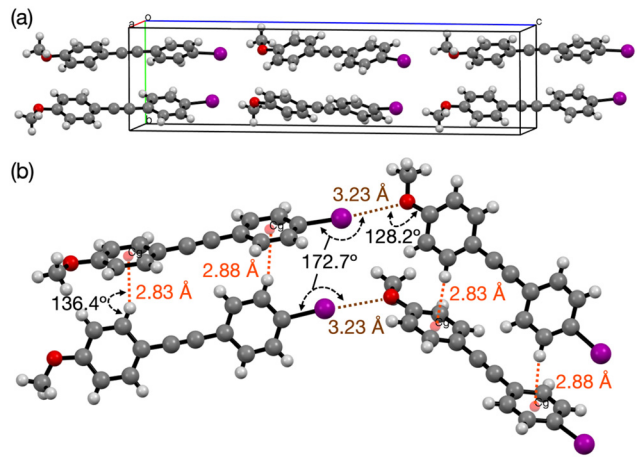

Fig. 2 Crystal structure of **2b**: (a) unit cell and (b) molecular packing involving the key C–H/π interaction and C–I···O halogen bonding.

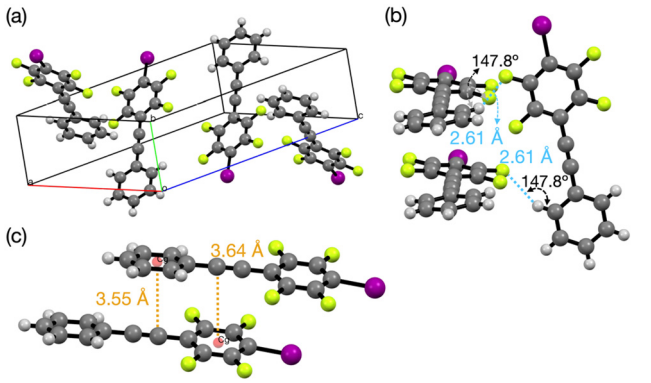

Fig. 3 Crystal structure of **2c**: (a) unit cell, (b) C–H···F interaction, and (c) alkyne–arene π–stacking interactions.

interaction. The π-stacking occurs between the alkyne moiety of one molecule and the fluorinated aromatic ring of an adjacent molecule, characterized by short contacts between alkyne carbon atoms and the ring centroid (Fig. 3c, C···Cg: 3.55–3.64 Å). The molecules are further connected by intermolecular C–H···F interaction. This interaction meets the geometric criteria for C–H···F interaction, with an H···F distance of 2.61 Å (shorter than the sum of the van der Waals radii, 2.67 Å) and C–H···F angle of 147.8° (Fig. 3b). For comparison, the previously reported structure of compound **1** (ref. 26) revealed the presence of both C–H···F and halogen bonding interactions (Fig. 4a and b). To comprehensively investigate differences in the intermolecular interactions between **1** and **2a–c**, Hirshfeld surface analysis was performed to quantify the contribution of each contact type to the total molecular surface (Fig. 5). In **2a**, H···C contacts, representing contributions from C–H/π systems,

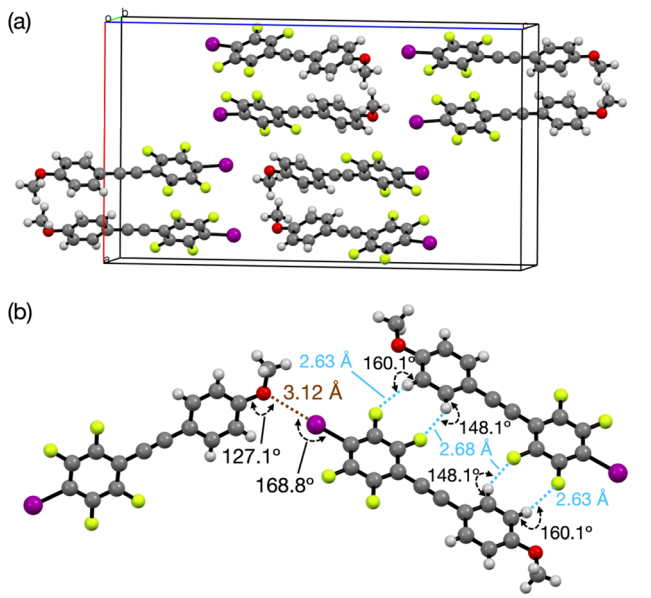

Fig. 4 Crystal structure of **1**: (a) unit cell and (b) intermolecular interactions, including C–H···F interaction and O···I halogen bonding, reported in ref. 26.

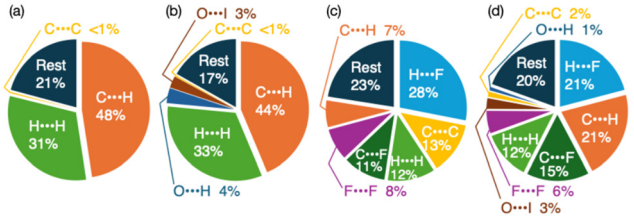

Fig. 5 Surface contact areas resulting from the Hirshfeld surface analyses of (a) **2a**, (b) **2b**, (c) **2c**, and (d) **1**.

were the most significant, accounting for approximately half of the surface. For **2b**, while H···C contacts remain dominant, significant contributions from O···I (halogen bonding) and O···H contacts are also observed. In the fluorinated analogue **2c**, H···F contacts (C–H···F interaction) become the primary contributor. Reference compound **1** is attributed to the synergistic effect of two highly directional interactions: O···I halogen bonding and significant contribution from C–H···F interaction. This unique combination creates a rigid intermolecular network that is absent in the other derivatives.

Cyclic voltammetry

CV measurements were conducted in acetonitrile to estimate the electronic properties of compounds **1** and **2a–c** (Fig. 6). The energy levels of the frontier orbitals were calculated based on the onset potentials obtained from the cyclic voltammograms (Table 1). The HOMO and LUMO of **2a** were estimated to be −6.24 and −2.51 eV, respectively, yielding an energy gap (ΔE) of 3.73 eV. In compound **2b**, introducing an electron-donating methoxy group resulted in destabilization of the HOMO level to −5.86 eV, while the LUMO level remained nearly unchanged. Consequently, the ΔE decreased to 3.30 eV. In compound **2c**, which contains electron-withdrawing fluorine atoms, both the HOMO and LUMO levels were more stable than those of **2a**. However, the LUMO was significantly more stabilized owing to the more extensive delocalization of its orbital, resulting in a decreased ΔE value,

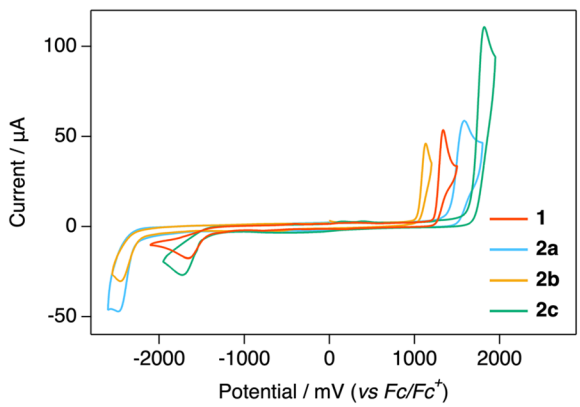

Fig. 6 Cyclic voltammograms of **1** and **2a–c** in an acetonitrile solution (10^{-3} mol L^{-1}).

Table 1 Orbital energies and relative parameters of **1** and **2a–c** obtained from the CV results

	HOMO [eV]	LUMO [eV]	ΔE [eV]
1	−6.06	−3.35	2.71
2a	−6.24	−2.51	3.73
2b	−5.86	−2.56	3.30
2c	−6.50	−3.30	3.20

similar to that of **2b**. Compound **1**, which includes both methoxy and fluorine substituents, demonstrated the lowest ΔE value among all the derivatives. This result was attributed to the combined effect of the methoxy group (increasing the HOMO energy) and fluorine atoms (decreasing the LUMO energy).

In addition to the orbital energies derived from the potentials, the peak current intensities also provided key insights. The peak current for fluorinated derivative **2c** was significantly higher than those of **2a** and **2b**. We hypothesize that this is due to the pre-aggregation of **2c** in 10^{-3} mol L^{-1} acetonitrile solution or its adsorption onto the electrode surface, induced by intermolecular interactions with the fluorine atoms. This hypothesis was further supported by a comparison with compound **1**. Although compound **1** also contains fluorine atoms, the current was not enhanced. We attribute this difference to the presence of the methoxy group in **1**, which likely improves solvation and, thus, counteracts the tendency for aggregation that might otherwise be induced by the fluorine atoms.

Photophysical properties in dilute solutions

UV-vis absorption and PL were measured in a 10^{-5} mol L^{-1} hexane solution (Fig. 7, Table 2). Compound **2a** exhibited a maximum absorption wavelength of 289 nm and multiple absorption peaks in the longer-wavelength region (Fig. 7a). The spectral shape of **2b** was similar to that of **2a**; however, it displayed a longer wavelength shift. This observation was consistent with the decreased ΔE value caused by the methoxy group, as confirmed by the CV results.

The fluorinated compounds **2c** and **1** exhibited similar spectral shapes; however, **1** exhibited a longer wavelength shift than **2c**, which was analogous to the trend observed between **2a** and **2b**. Notably, all compounds exhibited near-UV emissions, with an emission maximum at approximately 330 nm following excitation at their maximum absorption wavelength. A correlation between the emission maxima (λ_{PL}) and ΔE value estimated from CV was also observed. The absolute PL quantum yield (Φ_{PL}) of all compounds was <0.01, which was too low for observation with the naked eye. This weak emission was likely due to a non-radiative decay pathway involving a transition to a trans-bent state.[35,36]

Photophysical properties of the crystals

The emission spectra of **1** and **2a–c** were measured in the crystalline state (Fig. 8a, Table 3). All compounds exhibited dual

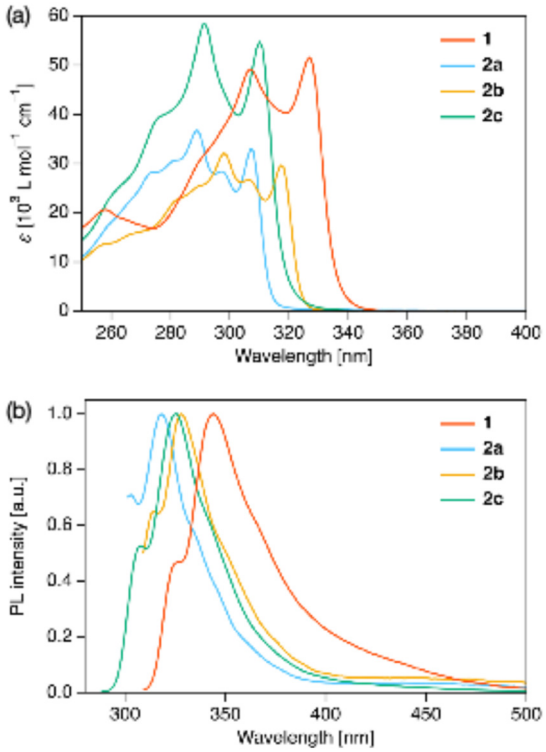

Fig. 7 (a) UV-vis absorption and (b) PL spectra of **1** and **2a–c** in 10^{-5} mol L^{-1} hexane obtained at a maximum absorption wavelength.

Table 2 Photophysical properties **1** and **2a–c** in 10^{-5} mol L^{-1} hexane

	λ_{abs} [nm] (ε [L mol^{-1} cm^{-1}])	λ_{PL} [a] [nm]	Φ_{PL} [b]
1	307 (49.2), 327 (51.6)	344	<0.01
2a	289 (36.3), 297 (28.4), 307 (33.1)	322	<0.01
2b	298 (32.1), 306 (26.7), 317 (29.6)	334	<0.01
2c	291 (58.3), 310 (54.8)	325	<0.01

[a] Excited at λ_{abs}. [b] Calculated using an integrating sphere.

emission maxima at approximately 400 and 500 nm. Time-resolved measurements revealed that the emission at approximately 400 nm had nanosecond or less lifetimes, which is characteristic of fluorescence (τ_{flu}) (Fig. S5–S7). Conversely, the emission at approximately 500 nm exhibited microsecond-range lifetimes, corresponding to phosphorescence (τ_{phos}). To further compare the fluorescence and phosphorescence of these crystals, the fluorescence intensities (I_{flu}) were normalized (Fig. 8b, inset). Compound **2a** exhibited extremely weak phosphorescence intensity (I_{phos}) with respect to the fluorescence intensity (I_{flu}), whereas **2b** showed a slight improvement. Conversely, the fluorinated compounds **2c** and **1** exhibited significantly enhanced I_{phos}, with phosphorescence intensity exceeding that of fluorescence. The PL quantum efficiency (Φ_{PL}) for **1** and **2c** were higher than those for **2a** and **2b**, indicating that introducing fluorine atoms enhanced both I_{phos} and the overall PL efficiency. The ratio of phosphorescence-to-fluorescence intensities (I_{phos}/I_{flu}) for

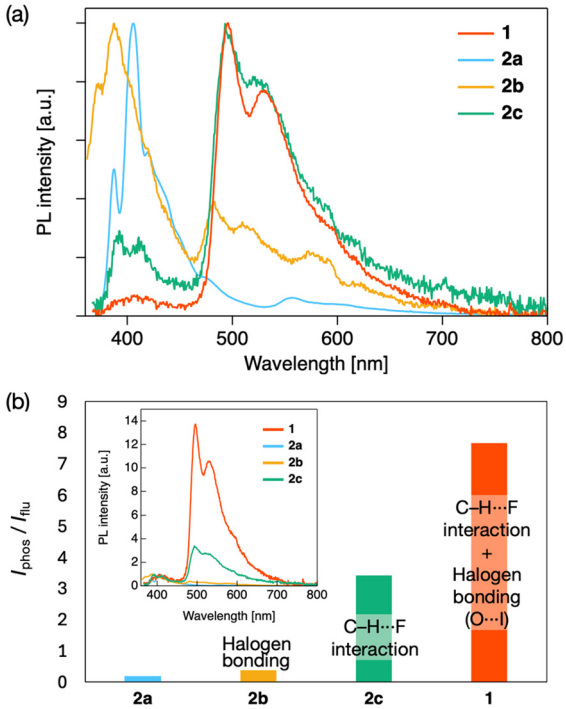

Fig. 8 (a) PL spectra excited at 360 nm. (b) Phosphorescence intensity of **1** and **2a–c** in the crystalline state.

compounds **1** and **2a–c**, as well as their intermolecular interactions, are summarized in Fig. 8b. Based on the Hirshfeld surface analysis (Fig. 5), the improvement in I_{phos} from **2a** to **2b** was attributed to the restriction of molecular motion due to O···I halogen bonding. The further enhancement observed for **2c** can be explained by the presence of C–H···F interactions.

To provide theoretical support for these findings, density functional theory calculations were performed based on the single-crystal geometry to estimate the frontier orbital energies in the solid state (see SI, Fig. S15 and Table S4 for details). Ultimately, the synergistic effect of both C–H···F and halogen bonding interactions in compound **1** resulted in the most significant overall improvement in its RTP properties.

Conclusions

This study systematically examined the influence of intermolecular interactions, particularly C–H···F and halogen bonding interactions, on the RTP properties of **DPA** derivatives. We synthesized a series of **DPA** derivatives

Table 3 Photophysical properties **1** and **2a–c** in the crystalline state

	λ_{PL} [a] [nm]	τ_{flu} [b] [ns]	τ_{phos} [b] [μs]	Φ_{PL} [b]
1	387, 405, 559	1.1	8.6	0.12
2a	387, 405, 559	<1.0	2.3	0.01
2b	387, 482, 581	<1.0	5.2	0.03
2c	392, 493, 520	1.2	5.9	0.06

[a] Excited at 350 nm. [b] Calculated using an integrating sphere.

(**2a–c**) with varying substituents to demonstrate that both types of interactions contributed to RTP enhancement. In particular, C–H···F interaction involving fluorine atoms is a primary factor for improving both phosphorescence intensity and efficiency. Detailed crystallographic analyses confirmed that the fluorinated derivatives (**1** and **2c**) formed strong intermolecular C–H···F interactions, which effectively restricted molecular motion and facilitated efficient RTP. Although C–H···F interaction alone had a moderate effect, its combination with halogen bonding produced a synergistic enhancement in RTP behavior. These results deepen our understanding of how non-covalent interactions modulate the photophysical properties of organic crystals and provide valuable design strategies for the development of high-performance, metal-free phosphorescent materials.

Author contributions

M. M.: data curation, investigation, validation, visualization, writing (original draft preparation), and writing (review and editing); M. Y., T. K.: investigation and writing (review and editing); S. Y.: conceptualization, data curation, investigation, validation, visualization, funding acquisition, writing (original draft preparation), writing (review and editing), and project administration.

Conflicts of interest

The authors declare that they have no conflicts of interest.

Data availability

Supplementary information: The SI provides experimental details, NMR spectra of the new compounds, PL spectra, single-crystal X-ray diffraction data, and quantum chemical calculations. See DOI: **https://doi.org/10.1039/D5CE00690B**.

CCDC 2125408–2125410 (**2a–2c**) contain the supplementary crystallographic data for this paper.[37a–c]

The crystallographic data were deposited in the Cambridge Crystallographic Data Centre (CCDC) database (CCDC 2125408 for **2a**, 2125409 for **2b**, and 2125410 for **2c**). The crystal structure of **1** has already been reported by our group (CCDC 2116930).[26]

Acknowledgements

This work was supported by the research equipment shared through the MEXT Project for Promoting Public Utilization of Advanced Research Infrastructure (Program for Supporting Introduction of the New Sharing System; Grant Number JPMXS0421800222).

References

1 G. Hong, X. Gan, C. Leonhardt, Z. Zhang, J. Seibert, J. M. Busch and S. Bräse, *Adv. Mater.*, 2021, **33**, e2005630, DOI: **10.1002/adma.202005630**.
2 P. L. dos Santos, P. Stachelek, Y. Takeda and P. Pander, *Mater. Chem. Front.*, 2024, **8**, 1731–1766, DOI: **10.1039/D3QM01067H**.
3 T. T. Bui, F. Goubard, M. Ibrahim-Ouali, D. Gigmes and F. Dumur, *Beilstein J. Org. Chem.*, 2018, **14**, 282–308, DOI: **10.3762/bjoc.14.18**.
4 L. Luo and Z. Liu, *VIEW*, 2022, **3**, 20200115, DOI: **10.1002/VIW.20200115**.
5 J. Chen, W. Zhang, L. Wang and G. Yu, *Adv. Mater.*, 2023, **35**, e2210772, DOI: **10.1002/adma.202210772**.
6 J. Mei, Y. Diao, A. L. Appleton, L. Fang and Z. Bao, *J. Am. Chem. Soc.*, 2013, **135**, 6724–6746, DOI: **10.1021/ja400881n**.
7 Z. Chen, S. Duan, X. Zhang and W. Hu, *Mater. Chem. Front.*, 2024, **8**, 2227–2272, DOI: **10.1039/D3QM01281F**.
8 S. Yuvaraja, A. Nawaz, Q. Liu, D. Dubal, S. G. Surya, K. N. Salama and P. Sonar, *Chem. Soc. Rev.*, 2020, **49**, 3423–3460, DOI: **10.1039/c9cs00811j**.
9 A. J. C. Kuehne and M. C. Gather, *Chem. Rev.*, 2016, **116**, 12823–12864, DOI: **10.1021/acs.chemrev.6b00172**.
10 Y. Jiang, Y. Y. Liu, X. Liu, H. Lin, K. Gao, W. Y. Lai and W. Huang, *Chem. Soc. Rev.*, 2020, **49**, 5885–5944, DOI: **10.1039/d0cs00037j**.
11 Q. Zhang, W. Tao, J. Huang, R. Xia and J. Cabanillas-Gonzalez, *Adv. Photonics Res.*, 2021, **2**, 2000155, DOI: **10.1002/adpr.202000155**.
12 X. D. Wang, O. S. Wolfbeis and R. J. Meier, *Chem. Soc. Rev.*, 2013, **42**, 7834–7869, DOI: **10.1039/c3cs60102a**.
13 E. Hemmer, P. Acosta-Mora, J. Méndez-Ramos and S. Fischer, *J. Mater. Chem. B*, 2017, **5**, 4365–4392, DOI: **10.1039/c7tb00403f**.
14 H. Uoyama, K. Goushi, K. Shizu, H. Nomura and C. Adachi, *Nature*, 2012, **492**, 234–238, DOI: **10.1038/nature11687**.
15 T. Ogawa, W. M. C. Sameera, D. Saito, M. Yoshida, A. Kobayashi and M. Kato, *Inorg. Chem.*, 2018, **57**, 14086–14096, DOI: **10.1021/acs.inorgchem.8b01654**.
16 Y. You, S. Cho and W. Nam, *Inorg. Chem.*, 2014, **53**, 1804–1815, DOI: **10.1021/ic4013872**.
17 B. Zhou, Q. Zhao, L. Tang and D. Yan, *Chem. Commun.*, 2020, **56**, 7698–7701, DOI: **10.1039/d0cc02730h**.
18 J. Li, X. Wang, Y. Pan, Y. Sun, G. Wang and K. Zhang, *Chem. Commun.*, 2021, **57**, 8794–8797, DOI: **10.1039/d1cc04094d**.
19 Y. Hong, J. W. Y. Lam and B. Z. Tang, *Chem. Commun.*, 2009, 4332–4353, DOI: **10.1039/b904665h**.
20 Y. Hong, J. W. Y. Lam and B. Z. Tang, *Chem. Soc. Rev.*, 2011, **40**, 5361–5388, DOI: **10.1039/c1cs15113d**.
21 W. Z. Yuan, X. Y. Shen, H. Zhao, J. W. Y. Lam, L. Tang, P. Lu, C. Wang, Y. Liu, Z. Wang, Q. Zheng, J. Z. Sun, Y. Ma and B. Z. Tang, *J. Phys. Chem. C*, 2010, **114**, 6090–6099, DOI: **10.1021/jp909388y**.
22 O. Bolton, K. Lee, H. J. Kim, K. Y. Lin and J. Kim, *Nat. Chem.*, 2011, **3**, 205–210, DOI: **10.1038/nchem.984**.
23 S. d'Agostino, F. Grepioni, D. Braga and B. Ventura, *Cryst. Growth Des.*, 2015, **15**, 2039–2045, DOI: **10.1021/acs.cgd.5b00226**.
24 J. Tong, Y. J. Wang, Z. Wang, J. Z. Sun and B. Z. Tang, *J. Phys. Chem. C*, 2015, **119**, 21875–21881, DOI: **10.1021/acs.jpcc.5b06088**.

25 S. Menning, M. Krämer, B. A. Coombs, F. Rominger, A. Beeby, A. Dreuw and U. H. F. Bunz, *J. Am. Chem. Soc.*, 2013, **135**, 2160–2163, DOI: **10.1021/ja400416r**.
26 M. Morita, S. Yamada and T. Konno, *New J. Chem.*, 2022, **46**, 4562–4569, DOI: **10.1039/D1NJ05539A**.
27 H. Li, D. R. Powell, T. K. Firman and R. West, *Macromolecules*, 1998, **31**, 1093–1098, DOI: **10.1021/ma971126s**.
28 M. Irfan, I. Sumra, M. Zhang, Z. Song, T. Liu and Z. Zeng, *Dyes Pigm.*, 2021, **190**, 109272, DOI: **10.1016/j.dyepig.2021.109272**.
29 M. G. Sarwar, B. Dragisic, L. J. Salsberg, C. Gouliaras and M. S. Taylor, *J. Am. Chem. Soc.*, 2010, **132**, 1646–1653, DOI: **10.1021/ja9086352**.
30 J. C. Collings, J. M. Burke, P. S. Smith, A. S. Batsanov, J. A. K. Howard and T. B. Marder, *Org. Biomol. Chem.*, 2004, **2**, 3172–3178, DOI: **10.1039/b411191e**.
31 G. M. Sheldrick, *Acta Crystallogr., Sect. A: Found. Adv.*, 2015, **71**, 3–8, DOI: **10.1107/S2053273314026370**.
32 G. M. Sheldrick, *Acta Crystallogr., Sect. C: Struct. Chem.*, 2015, **71**, 3–8, DOI: **10.1107/S2053229614024218**.
33 O. V. Dolomanov, L. J. Bourhis, R. J. Gildea, J. A. K. Howard and H. Puschmann, *J. Appl. Crystallogr.*, 2009, **42**, 339–341, DOI: **10.1107/S0021889808042726**.
34 E. Pidcock, *Chem. Commun.*, 2005, 3457–3459, DOI: **10.1039/B505236J**.
35 M. Z. Zgierski and E. C. Lim, *Chem. Phys. Lett.*, 2004, **387**, 352–355, DOI: **10.1016/j.cplett.2004.02.029**.
36 J. Saltiel and V. K. R. Kumar, *J. Phys. Chem. A*, 2012, **116**, 10548–10558, DOI: **10.1021/jp307896c**.
37 (*a*) M. Morita, M. Yasui, T. Konno and S. Yamada, CCDC 2125408: Experimental Crystal Structure Determination, 2025, DOI: **10.5517/ccdc.csd.cc29bnkw**; (*b*) M. Morita, M. Yasui, T. Konno and S. Yamada, CCDC 2125409: Experimental Crystal Structure Determination, 2025, DOI: **10.5517/ccdc.csd.cc29bnlx**; (*c*) M. Morita, M. Yasui, T. Konno and S. Yamada, CCDC 2125410: Experimental Crystal Structure Determination, 2025, DOI: **10.5517/ccdc.csd.cc29bnmy**.